

Bispectrum and Nonlinear Biasing of Galaxies: Perturbation Analysis, Numerical Simulation and SDSS Galaxy Clustering

Takahiro NISHIMICHI¹, Issha KAYO², Chiaki HIKAGE², Kazuhiro YAHATA¹,
Atsushi TARUYA¹, Y. P. JING³, Ravi K. SHETH⁴, and, Yasushi SUTO¹

¹*Department of Physics, School of Science, The University of Tokyo, Tokyo 113-0033*

²*Department of Physics and Astrophysics, Nagoya University, Chikusa, Nagoya 464-8602*

³*The Partner Group of MPI fur Astrophysik, Shanghai Astronomical Observatory,
Nandan Road 80, Shanghai 200030, China*

⁴*Department of Physics & Astronomy, University of Pennsylvania, PA 19130, USA
nishimichi@utap.phys.s.u-tokyo.ac.jp*

(Received 2006 0; accepted 2006 0)

Abstract

We consider nonlinear biasing models of galaxies with particular attention to a correlation between linear and quadratic biasing coefficients, b_1 and b_2 . We first derive perturbative expressions for b_1 and b_2 in halo and peak biasing models. Then we compute

power spectra and bispectra of dark matter particles and halos using N-body simulation data and of volume-limited subsamples of Sloan Digital Sky Survey (SDSS) galaxies, and determine their b_1 and b_2 . We find that the values of those coefficients at linear regimes ($k < 0.2h\text{Mpc}^{-1}$) are fairly insensitive to the redshift-space distortion and the survey volume shape. The resulting normalized amplitudes of bispectra, Q , for equilateral triangles, are insensitive to the values of b_1 implying that b_2 indeed correlates with b_1 . The present results explain the previous finding of Kayo et al. (2004) for the hierarchical relation of three-point correlation functions of SDSS galaxies. While the relations between b_1 and b_2 are quantitatively different for specific biasing models, their approximately similar correlations indicate a fairly generic outcome of the biasing due to the gravity in primordial Gaussian density fields.

Key words: cosmology: large-scale structure of universe — observations — theory — methods: statistical

1. Introduction

One of the major uncertainties in precise cosmology is the galaxy biasing relative to the underlying mass distribution. It hampers extracting the cosmological information from the large scale structure of the universe. In particular, the biasing is sensitive to the unknown physical conditions of galaxy formation. Thus its phenomenological parameterization and understanding is crucial in advancing our knowledge of the evolution of the universe.

A reasonable approximation often adopted is a local linear biasing model, which assumes a simple scale-independent relation between the density contrast fields of galaxy and mass:

$$\delta_g(\mathbf{x}, z) = b(z)\delta(\mathbf{x}, z). \quad (1)$$

In the above, the density contrast of the mass is defined as

$$\delta(\mathbf{x}, z) \equiv \frac{\rho(\mathbf{x}, z) - \bar{\rho}(z)}{\bar{\rho}(z)}, \quad (2)$$

where the over-bar indicates the mean over the entire universe. The number density contrast of galaxy density field, δ_g , is defined similarly. Because this model contains only a single time-dependent parameter $b(z)$, it is not surprising that the model cannot describe the observed features of galaxy clustering accurately. Furthermore, the three-point correlation function of SDSS galaxies (Kayo et al. 2004) indicates the importance of the higher-order correction to equation (1); while the galaxy two-point correlation functions are well represented by the linear biasing model (e.g., Zehavi et al. 2005), the normalized amplitudes Q of the corresponding three-point functions do not show the expected scaling with respect to $b(z)$:

$$Q \propto \frac{1}{b}. \quad (3)$$

In reality, however, Q of SDSS galaxies in redshift space proves to be almost scale-independent, and follows the

hierarchical relation approximately, $Q = 0.5 \sim 1.0$. Moreover its dependence on the morphology, color, and luminosity is not statistically significant. Given the robust morphological, color and luminosity dependences of the two-point correlation function, Kayo et al. (2004) argued that galaxy biasing is complex and requires a contrived relation between the linear biasing and its higher order correction terms. Another possibility is that the observed value is significantly contaminated by the redshift-space distortion and does not properly reflect the actual clustering information in real space. Indeed the previous N-body studies of the redshift-space distortion on three- and four-point correlation functions suggest that this is the case in nonlinear regimes (Suto 1993; Matsubara & Suto 1994; Suto & Matsubara 1994). The interpretation is further complicated by the fact that the higher-order statistics is sensitive to relatively rare large-scale structures in particular samples (Nichol et al. 2006).

The main purpose of the present paper is to provide a physical explanation for the approximate hierarchical relation for Q of SDSS galaxy clustering on the basis of perturbation analysis and numerical simulations. This is a step toward the understanding of the nonlinear nature of biasing. Specifically we employ a local *nonlinear* biasing model (Fry & Gaztanaga 1993):

$$\delta_b(\mathbf{x}, z) = \sum_{n=0}^{\infty} \frac{b_n(z)}{n!} [\delta(\mathbf{x}, z)]^n. \quad (4)$$

We consider density peaks, dark matter halos, simulated halos, and the SDSS galaxies as specific examples for the density fields δ_b in the left hand side.

The outline of the paper is as follows; section 2 briefly summarizes the halo and peak biasing models as analytically tractable examples. We compute the linear and quadratic biasing coefficients perturbatively and find that these models roughly agree with the observed hierarchical relation. To be more realistic, we analyze simulated halo catalogs and SDSS galaxies in section 3, and find that the perturbative result is valid even if we take account of a variety of selection effects and particularly redshift-space distortion. The quantitative agreement between the two indicates a generic correlation among the biasing coefficients in the SDSS galaxies. Finally, section 4 is devoted to the summary and conclusion of the paper.

2. Perturbative predictions in halo and peak biasing models

2.1. Basic statistics and perturbation biasing models

Throughout the present analysis, we work in the Fourier space. For definiteness, we adopt the definition of the Fourier transform of an arbitrary function $g(\mathbf{x})$ as

$$g(\mathbf{k}) \equiv \int \frac{d^3\mathbf{x}}{(2\pi)^3} g(\mathbf{x}) e^{-i\mathbf{k}\cdot\mathbf{x}}. \quad (5)$$

Then the power spectrum and the bispectrum of the mass density field are defined as

$$\langle \delta(\mathbf{k}_1) \delta(\mathbf{k}_2) \rangle \equiv P(k_1) \delta_D(\mathbf{k}_1 + \mathbf{k}_2), \quad (6)$$

$$\langle \delta(\mathbf{k}_1) \delta(\mathbf{k}_2) \delta(\mathbf{k}_3) \rangle \equiv B(k_1, k_2, k_3) \delta_D(\mathbf{k}_1 + \mathbf{k}_2 + \mathbf{k}_3), \quad (7)$$

where δ_D denotes the Dirac delta and we assume the universe is isotropic and homogeneous. We introduce the normalized amplitude of the mass bispectrum as

$$Q_m(k_1, k_2, k_3) \equiv \frac{B(k_1, k_2, k_3)}{P(k_1)P(k_2) + P(k_2)P(k_3) + P(k_3)P(k_1)}. \quad (8)$$

Note that strictly speaking, the above statistic is different from that defined in configuration space¹. Since both are expected to be nearly identical in a weakly nonlinear regime, we focus on the Fourier space analysis throughout this paper (see also Verde et al. 2002 and Hikage et al. 2005). The analysis in configuration space is now in progress.

The above statistics can be generalized in a straightforward manner to any biased field. If one keeps the linear and quadratic terms in equation (4), one obtains

$$P_b(k) = b_1^2 P(k), \quad (9)$$

$$Q_b(k_1, k_2, k_3) = \frac{1}{b_1} \left[Q_m(k_1, k_2, k_3) + \frac{b_2}{b_1} \right]. \quad (10)$$

Therefore, Q_b for the biased field is directly dependent on the quadratic biasing coefficient b_2 unlike in the case of the power spectrum. As we show below, this term plays an important role to approximately satisfy the hierarchical

¹ In this paper, we use the term ‘‘real space’’ in order to imply the analysis without redshift-space distortion in k-space. Thus we reserve the term ‘‘configuration space’’ in order to distinguish from k-space.

relation. In order to understand the qualitative relations among the biasing coefficients, we first consider analytically workable biasing models, i.e., halo and peak biasing.

2.2. Halo biasing

We follow the formalism of Mo & White (1996) for halo biasing. We define (unconditional) mass function, $n_{\text{halo}}(m, z)$ of halos with mass m at redshift z . We rewrite the unconditional mass function as

$$\frac{m^2 n_{\text{halo}}(m, z)}{\bar{\rho}} \frac{dm}{m} = \nu f(\nu) \frac{d\nu}{\nu}, \quad \nu(m, z) \equiv \delta_{\text{sc}}(z)/\sigma(m). \quad (11)$$

We denote by $\sigma(m)$ the linearly extrapolated value of the rms of the initial density fluctuation field smoothed with a tophat filter of scale $R = (3m/4\pi\bar{\rho})^{1/3}$, where $\bar{\rho}$ is the mean comoving background density. The characteristic density contrast for spherical collapse is given as

$$\delta_{\text{sc}}(z) \simeq \frac{3(12\pi)^{2/3}}{20} [1 + 0.0123 \log_{10} \Omega_m(z)] / D(z), \quad (12)$$

where $\Omega_m(z)$ is the matter density in units of the critical density at redshift z , and $D(z)$ is the linear growth rate (Kitayama & Suto 1996). In the above equation and throughout the paper, we assume a spatially-flat model with non-vanishing cosmological constant. Specifically, we adopt the present value of mass density $\Omega_m = 0.3$, the cosmological constant $\Omega_\Lambda = 0.7$, the Hubble constant $h = H_0/(100 \text{ km s}^{-1} \text{ Mpc}^{-1}) = 0.7$, and the amplitude of the density fluctuations smoothed over $8h^{-1} \text{ Mpc}$ $\sigma_8 = 0.9$.

There exist two popular models for $f(\nu)$. One is based on a spherical collapse model (Press & Schechter 1974):

$$\nu f_{\text{PS}}(\nu) = 2\sqrt{\frac{\nu^2}{2\pi}} \exp(-\nu^2/2). \quad (13)$$

The other is based on an ellipsoidal collapse model (Sheth & Tormen 1999):

$$\nu f_{\text{ST}}(\nu) = 2A(p) \left(1 + \frac{1}{(q\nu^2)^p}\right) \sqrt{\frac{q\nu^2}{2\pi}} \exp(-q\nu^2/2), \quad (14)$$

where $p \approx 0.3$, $A(p) = [1 + 2^{-p}\Gamma(1/2 - p)/\sqrt{\pi}]^{-1} \approx 0.3222$, and $q \approx 0.75$ (Cooray & Sheth 2002).

Consider a comoving volume V and its total mass M at redshift z_0 . Let $n_{\text{halo}}(m, z_1 | M, V, z_0) dm$ denote the conditional number density of halos whose mass is between m and $m + dm$ at z_1 . A reasonable approximation for $n_{\text{halo}}(m, z_1 | M, V, z_0)$ is obtained by applying the extended Press-Schechter theory (e.g., Bower 1991; Bond et al. 1991):

$$\frac{m^2 n_{\text{halo}}(m, z_1 | M, V, z_0)}{\bar{\rho}} \frac{dm}{m} = \nu_{10} f(\nu_{10}) \frac{d\nu_{10}}{\nu_{10}}, \quad (15)$$

$$\nu_{10} = \frac{\delta_{\text{sc}}(z_1) - \delta_0(z_0)}{\sqrt{\sigma^2(m) - \sigma^2(M)}}, \quad (16)$$

where $\delta_0(z_0)$ is the linearly extrapolated mass density contrast at z_0 . If we define the actual density contrast $\delta = M/(\bar{\rho}V) - 1$, $\delta_0(z_0)$ is written as

$$\frac{\delta_0}{1 + z_0} = \sum_{i=0}^{\infty} a_i \delta^i, \quad (17)$$

$$a_0 = 0; \quad a_1 = 1; \quad a_2 = -\frac{17}{21}; \quad a_3 = \frac{341}{567}; \quad a_4 = -\frac{55805}{130977}; \quad \dots, \quad (18)$$

where the above coefficients are obtained assuming the spherical collapse model (Bernardeau 1994).

Now one can write down the corresponding conditional density contrast of halos:

$$\delta_{\text{halo}}(m, z_1 | M, V, z_0) = \frac{n_{\text{halo}}(m, z_1 | M, V, z_0)(1 + \delta)}{n_{\text{halo}}(m, z_1)} - 1. \quad (19)$$

Expanding equation (19) in terms of δ_0 in the limit of $\sigma(M) \rightarrow 0$ yields the biasing coefficients of halos (Mo, Jing & White 1997; Cooray & Sheth 2002):

$$\begin{aligned} b_1(m, z) &= 1 + \epsilon_1 + E_1, \\ b_2(m, z) &= 2(1 + a_2)(\epsilon_1 + E_1) + \epsilon_2 + E_2, \end{aligned} \quad (20)$$

where

$$\epsilon_1 = \frac{q\nu^2(m, z) - 1}{\delta_{\text{sc}}(z)}, \quad \epsilon_2 = \frac{q\nu^2(m, z)}{\delta_{\text{sc}}(z)} \left(\frac{q\nu^2(m, z) - 3}{\delta_{\text{sc}}(z)} \right), \quad (21)$$

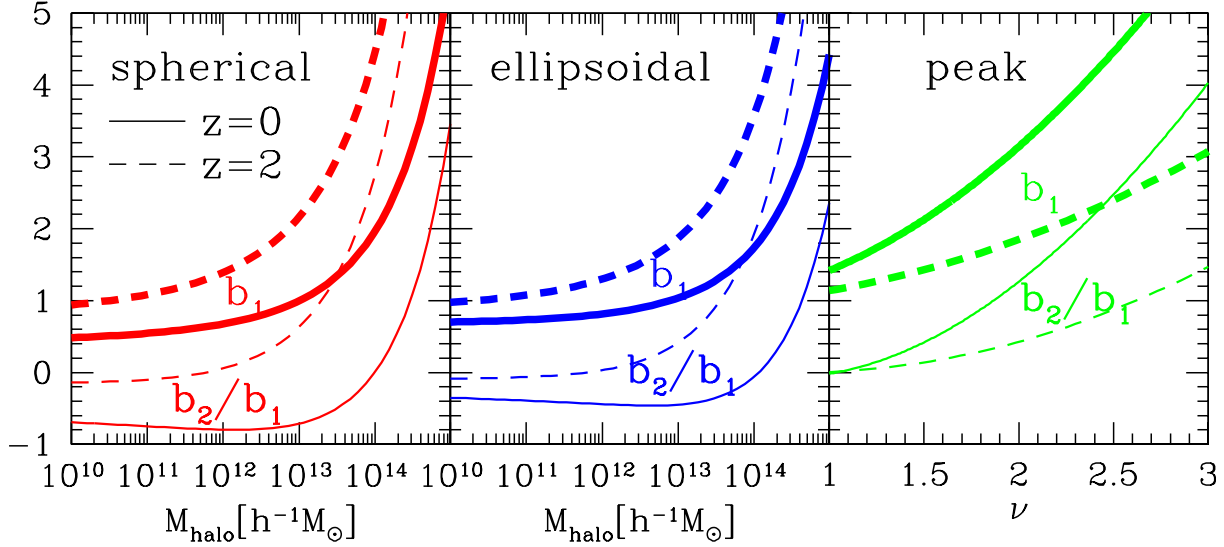


Fig. 1. biasing coefficients in the three perturbative biasing models. Thick and thin curves show b_1 and b_2/b_1 at $z=0$ (solid) and $z=2$ (dashed). We use spherical halo model (left), ellipsoidal halo model (center), and peak model (right). The biasing coefficients are plotted against halo mass M_{halo} (left and center), and against peak height ν (right).

$$E_1 = \frac{2p}{\delta_{\text{sc}}(z)[1 + (qv^2(m, z))^p]}, \quad \frac{E_2}{E_1} = \frac{1 + 2p}{\delta_{\text{sc}}(z)} + 2\epsilon_1. \quad (22)$$

The above results for ellipsoidal collapse reduce to those for spherical collapse, if one sets $p=0$ and $q=1$.

2.3. Peak biasing

The biasing coefficients of the peak model can be obtained similarly as the halo model described in the above subsection. The conditional and unconditional number densities of peaks with peak height $\nu \equiv \delta/\sigma$ are derived in Bardeen et al. (1986). In this case, σ denotes the rms value of density fluctuation smoothed over $R \equiv (3m/4\pi\bar{\rho})^{1/3}$, and δ is the density contrast of the peaks in the smoothed field. Substituting those formulae into the right-hand side of equation (19), one similarly obtains the biasing coefficients for the peak model (Mo, Jing & White 1997):

$$b_1(\nu, z) = 1 + \frac{\nu^2 + g_1}{\delta_{\text{sc}}(z)}, \quad (23)$$

$$b_2(\nu, z) = 2(1 + a_2) \frac{\nu^2 + g_1}{\delta_{\text{sc}}(z)} + \left(\frac{\nu}{\delta_{\text{sc}}(z)} \right)^2 \left(\nu^2 - 1 + 2g_1 + \frac{2g_2}{\nu^2} \right), \quad (24)$$

where the above functions, g_1 and g_2 , are defined in equation (25) of Mo, Jing & White (1997).

2.4. Results of Analytic Models

We consider the above three models, spherical halo, ellipsoidal halo, and peak, to explore the correlation between b_1 and b_2 analytically.

Figure 1 shows biasing coefficients, b_1 (thick lines) and b_2/b_1 (thin lines) at $z=0$ (solid) and $z=2$ (dashed). We adopt the cold dark matter transfer function of Bardeen et al. (1986) as the initial mass power spectrum (with $\Omega_m = 0.3$, $\Omega_\Lambda = 0.7$, and the shape parameter $\Gamma = \Omega_m h = 0.21$). In the three biasing models, b_1 and b_2/b_1 behave similarly as functions of M_{halo} or ν . This implies a presence of a certain correlation between b_1 and b_2/b_1 . To see this point more clearly, we plot b_2/b_1 in terms of b_1 for each model (figure 2). All the three models exhibit very similar correlations between b_1 and b_2/b_1 . The differences among the three models become even smaller at higher redshifts; compare $z=0$ (thick lines) and $z=2$ (thin lines).

In analyzing simulation data below, the estimate of the biasing coefficients is made after averaging over a finite mass range. We calculate the mass-averaged values of b_1 and b_2 for halo models at $z=0$:

$$B_n(m_{\text{min}}, m_{\text{max}}) = \frac{\int_{m_{\text{min}}}^{m_{\text{max}}} dm n_{\text{halo}}(m, z=0) b_n(m, z=0)}{\int_{m_{\text{min}}}^{m_{\text{max}}} dm n_{\text{halo}}(m, z=0)}, \quad (n=1, 2). \quad (25)$$

The difference between b_n and B_n is illustrated in figure 2, where spherical (open) and ellipsoidal (filled) halo models

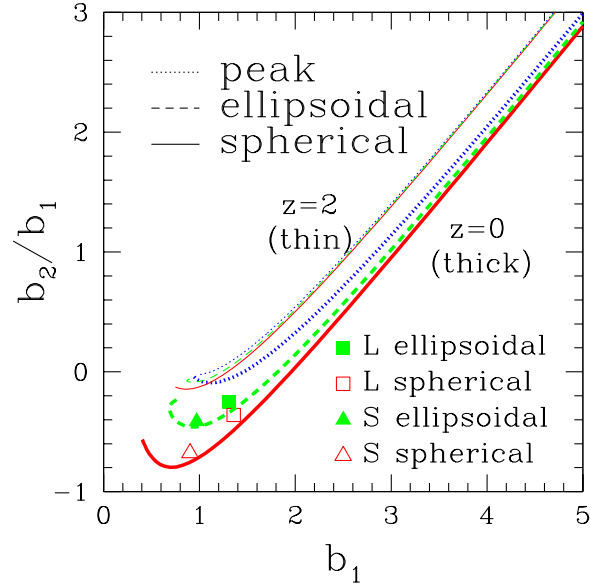


Fig. 2. Correlation of b_1 and b_2/b_1 from halo and peak biasing. Different line types are results of halo biasing of spherical collapse (solid), ellipsoidal collapse (dashed), and peak biasing (dotted), evaluated at redshifts 2 (thin) and 0 (thick). Open (filled) symbols represent the mass-averaged values, B_1 and B_2/B_1 , defined in equation (25), assuming spherical (ellipsoidal) halo model. The mass ranges correspond to L (square), and S (triangle) defined in subsection 3.1.

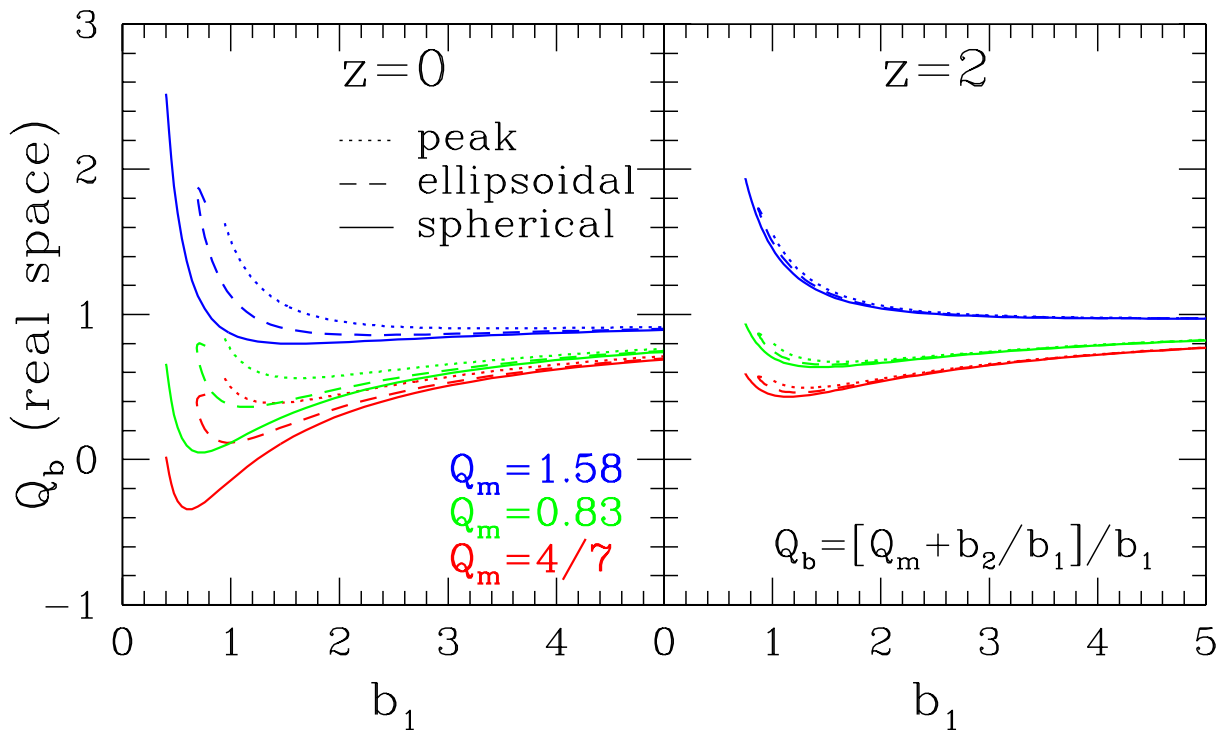


Fig. 3. Q for biased fields as a function of b_1 in real space. We estimate Q using equation (10) on the basis of perturbative predictions for peaks (dotted), ellipsoidal halos (dashed), and spherical halos (solid). We assume three different values for Q_m : $Q_m = 1.58$, $Q_m = 0.83$, and $Q_m = 4/7$ from top to bottom. The first two values are computed from N-body results at $k = 0.4h\text{Mpc}^{-1}$, and $k = 0.18h\text{Mpc}^{-1}$ (see section 3 below), and the last value corresponds to perturbation theory [eqs.(39) and (40)], where equilateral triangles ($k_1 = k_2 = k_3 = k$) are assumed. *left: $z = 0$, right: $z = 2$.*

[eqs.(13), (14)] are assumed. We plot the results for two mass ranges, corresponding to S (triangle) and L (square) halo subsamples (see subsection 3.1 for detail).

Figure 3 plots Q_b for biased fields as a function of b_1 in real space. The dotted, dashed and solid lines represent

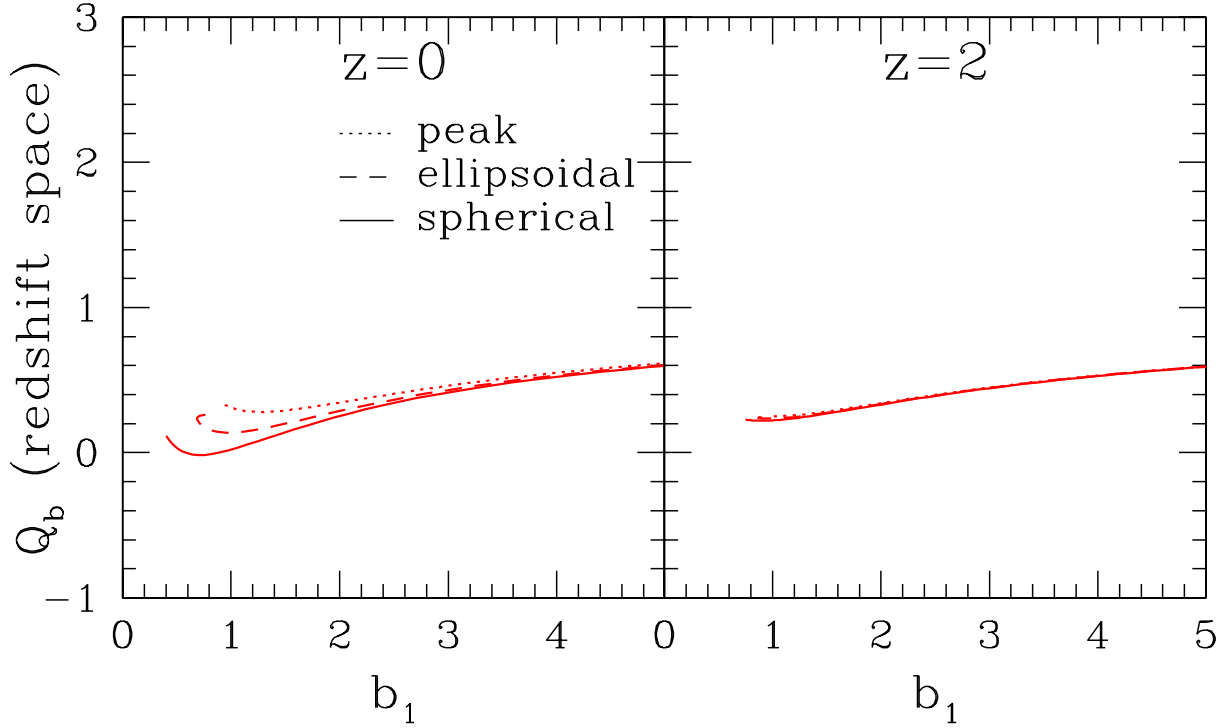


Fig. 4. Same as figure 3, but for redshift space. We use equation (26) for equilateral triangles instead of equation (10). In this time, Q_b is calculated directly (not in terms of Q_m), so we plot only one set corresponding to $Q_m = 4/7$ in figure 3.

the results of tree-level perturbation with respect to biasing, equation (10), for peak, ellipsoidal, and spherical halo models. For simplicity, we consider equilateral triangles and adopt three different values for Q_m ; $Q_m = 4/7$ from the leading term of the gravitational nonlinearity [see eq.(39) below], and $Q_m = 0.83$ and 1.58 from N-body results at $k = 0.18h\text{Mpc}^{-1}$ and $k = 0.40h\text{Mpc}^{-1}$.

Figure 4 plots Q_b for biased fields but in redshift space. The redshift distortion effect for Q is difficult to model accurately, and we follow Scoccimarro, Couchman & Frieman (1999) and replace equation (10) by

$$Q_{b,\text{seq}} = \frac{5(2520 + 4410\gamma + 1890\beta + 2940\gamma\beta + 378\beta^2 + 441\gamma\beta^2 + 9\beta^3 + 1470b_1\beta + 882b_1\beta^2 - 14b_1\beta^4)}{98b_1(15 + 10\beta + 3\beta^2)^2}, \quad (26)$$

$$\beta \equiv \frac{1}{b_1} \left[\Omega_m^{4/7} + \frac{\Omega_\Lambda}{70} \left(1 + \frac{\Omega_m}{2} \right) \right], \quad (27)$$

for equilateral triangles, with $\gamma \equiv b_2/b_1$.

These simple halo and peak biasing models imply that the nonlinearity of biasing weakens the dependence of Q_{halo} and Q_{peak} on b_1 , which qualitatively explains the results of Kayo et al. (2004). To be more realistic, however, we consider in the next section nonlinear gravity, redshift-space distortion and finite survey boundary effect using N-body simulations and SDSS data.

3. Comparison with N-body simulations and SDSS galaxies

3.1. N-body simulations and SDSS galaxies

N-body simulations that we use employ 512^3 dark matter particles in a cubic box of $300h^{-1}\text{Mpc}$ (comoving) on a side with the periodic boundary condition. The mass of each dark matter particle is $1.68 \times 10^{10}h^{-1}M_\odot$. As in section 2, we use the cold dark matter transfer function of Bardeen et al. (1986) as the initial mass power spectrum (with $\Omega_m = 0.3$, $\Omega_\Lambda = 0.7$, and $\Gamma = \Omega_m h = 0.21$), and have generated three independent Gaussian realizations. The initial density field at $z = 36$ is evolved up to $z = 0$ using the P³M code of Jing & Suto (1998, 2002) with the gravitational softening length of $\epsilon \sim 58h^{-1}\text{kpc}$.

In order to test the dependence of Q_b on actual galaxy properties, we construct volume-limited subsamples of different colors from New York University Value-Added Galaxy Catalog (Blanton et al. 2005) based on the SDSS Data Release 4 (Adelman-McCarthy et al. 2006). The angular selection function of the survey is written in terms of spherical polygons (Hamilton & Tegmark 2004). Details of the SDSS can be found in the following papers: York

Table 1. Volume-limited subsamples of SDSS galaxies for $0.05 < z < 0.1$.

subsample	luminosity	color	N_g	$n_g[h^3\text{Mpc}^{-3}]$	$2\pi n_g^{1/3}[h\text{Mpc}^{-1}]$	b_1
blue	$-21.3 < M_r < -19.8$	$g - r < 0.86$	33986	0.00359	0.962	0.95 ± 0.02
red	$-21.3 < M_r < -19.8$	$g - r > 0.86$	34351	0.00363	0.966	1.33 ± 0.10

Table 2. Subsamples of simulated halos.

subsample	$M[h^{-1}M_\odot]$	$\langle N_h \rangle$	$\langle n_h \rangle [h^3\text{Mpc}^{-3}]$	$2\pi \langle n_h \rangle^{1/3} [h\text{Mpc}^{-1}]$	$\langle b_1 \rangle$
r-cube S	$1.68 \times 10^{12} - 1.18 \times 10^{13}$	58692	0.00217	0.814	0.83 ± 0.01
r-cube L	$> 1.18 \times 10^{13}$	10881	0.000403	0.461	1.26 ± 0.02
r-cube LL	$> 6.72 \times 10^{13}$	1484	0.0000550	0.239	1.8 ± 0.1
s-cube S	$1.68 \times 10^{12} - 1.18 \times 10^{13}$	58692	0.00217	0.814	0.88 ± 0.01
s-cube L	$> 1.18 \times 10^{13}$	10881	0.000403	0.461	1.29 ± 0.01
s-cube LL	$> 6.72 \times 10^{13}$	1484	0.0000550	0.239	1.8 ± 0.1
wedge S	$1.68 \times 10^{12} - 1.18 \times 10^{13}$	21735	0.00230	0.829	0.84 ± 0.01
wedge L	$> 1.18 \times 10^{13}$	3979	0.000421	0.471	1.24 ± 0.09
wedge LL	$> 6.72 \times 10^{13}$	551	0.0000582	0.243	1.8 ± 0.2

et al. (2000) describe an overview, technical articles providing details include descriptions of the telescope design (Gunn et al. 2006), the photometric camera (Gunn et al. 1998), photometric analysis (Stoughton et al. 2002), the photometric system and calibration (Fukugita et al. 1996; Hogg et al. 2001; Ivezić et al. 2004; Smith et al. 2002; Tucker et al. 2006), the photometric pipeline (Lupton et al. 2001), astrometric calibration (Pier et al. 2003), selection of the galaxy spectroscopic samples (Eisenstein et al. 2001; Strauss et al. 2002), and spectroscopic tiling (Blanton et al. 2003).

We only consider galaxies with redshifts $0.05 \leq z \leq 0.1$ and magnitudes $-21.3 \leq M_r \leq -19.8$ (68337 galaxies in total, over $\sim 4259\text{deg}^2$). We divide those galaxies according to their colors so that each subsample contains roughly the same number: *red* subsample has $g - r > 0.86$ (34351 in total), and *blue* subsample has $g - r < 0.86$ (33986). In Table 1, N_g and n_g denote the total number of galaxies and the galaxy number density in each subsample. The wavenumber corresponding to the mean galaxy separation is $2\pi n_g^{1/3}$, and the linear biasing coefficient, b_1 is evaluated at $k = 0.126h\text{Mpc}^{-1}$.

In order to compare with analytical predictions for halo biasing and also with the SDSS subsamples, we identify dark matter halos using a friends-of-friends algorithm. Specifically we use the public code “FOF”², and adopt the linking length 0.164 in units of the mean particle separation. We construct nine halo subsamples from three realizations (Table 2). The indices, S, L, and LL, represent the three different halo mass ranges corresponding to $1.68 \times 10^{12}h^{-1}M_\odot < M < 1.18 \times 10^{13}h^{-1}M_\odot$, $1.18 \times 10^{13}h^{-1}M_\odot < M$, and $6.72 \times 10^{13}h^{-1}M_\odot < M$. The mass ranges of the first two, S and L, are determined so that they have approximately the same values of b_1 for the SDSS blue and red galaxies, respectively. The last one, LL, is constructed so as to check the b_2 - b_1 correlation around $b_1 \sim 2$, and discussed in figure 8 below. We further divide the three different mass-selected samples into three subsamples: r-cube (s-cube) measures positions of halos in real (redshift) space using the original simulation cube, $(300h^{-1}\text{Mpc})^3$. In the latter, redshift-space distortion effect is taken into account by using z -component of the center-of-mass velocity of each halo. Wedge subsamples are constructed so as to have the same survey geometry as the SDSS sample. They measure the positions of halos in redshift space, using the line-of-sight component of the center-of-mass velocity unlike s-cube. In Table 2, $\langle N_h \rangle$ and $\langle n_h \rangle$ denote the total number of halos and the halo number density in each subsample (averaged over three realizations). The wavenumber corresponding to the mean halo separation is $2\pi \langle n_h \rangle^{1/3}$, and the linear biasing coefficient, $\langle b_1 \rangle$ is evaluated at $k = 0.126h\text{Mpc}^{-1}$.

3.2. Power spectrum and b_1

First we estimate the linear biasing parameter according to equation (9):

$$b_{1,i}(k) = \sqrt{\frac{P_i(k)}{P(k)}}, \quad (28)$$

where the subscript i denotes the different subsamples of simulated halos and SDSS galaxies.

In real-space (r-cube in Table 2), we first construct density field of halos using the cloud-in-cell pixelization, Fourier transform it, angularly average $P_i(\mathbf{k})$ over the direction of \mathbf{k} , and finally remove the shot noise contribution, $1/n_h$ to obtain $P_i(k)$. We choose logarithmically equal bins for k , $\Delta(\log_{10} k) = 1/6$. The mean values $\langle n_h \rangle$ of the number density

² available at the website <http://www-hpcc.astro.washington.edu/>

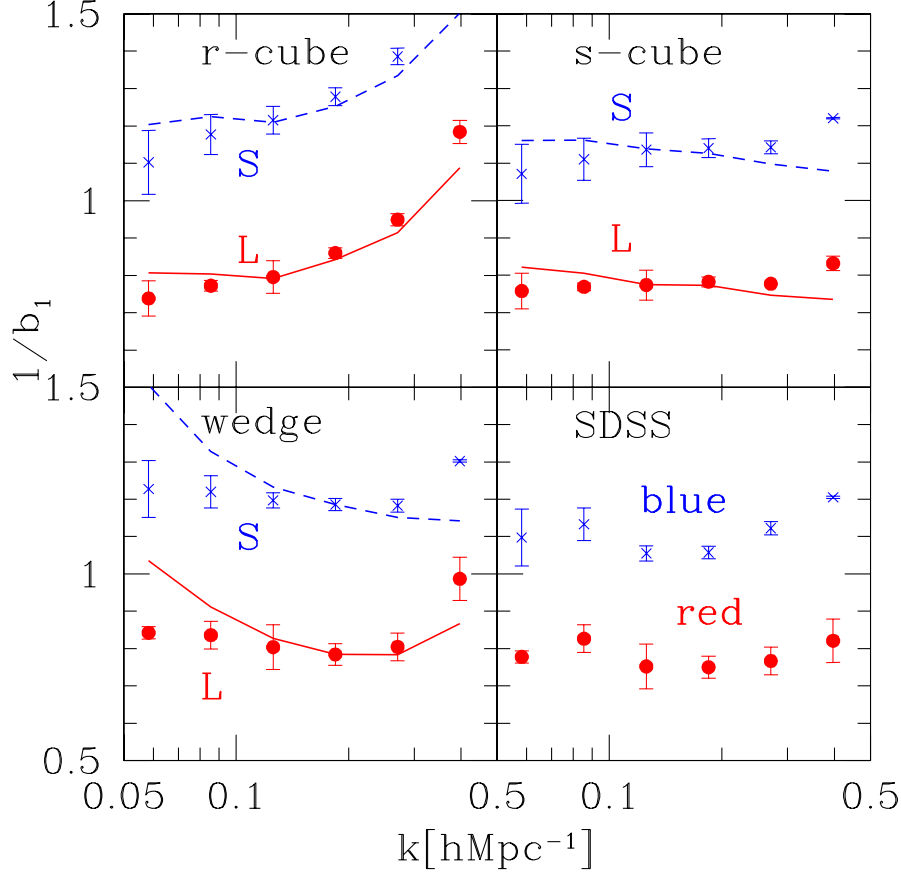


Fig. 5. Inverse of the linear biasing parameters of simulated halos (Table 2) and SDSS galaxies (Table 1). Crosses and filled circles for simulated halos (SDSS galaxies) correspond to S and L samples (blue and red), respectively. Dashed and solid lines in r-cube, s-cube, and wedge indicate results based on the direct estimation of $P(k)$, while symbols in all panels use $P^{\text{PD},r}(k)$ or $P^{\text{PD},s}(k)$, equation (29). The quoted error bars for simulated halos are computed from three different realizations. We simply use the error bars for wedge subsamples just for reference in the case of SDSS galaxies.

of halos in each realization (n_h) are listed in Table 2. The wavenumbers corresponding to the mean halo separation $2\pi/\langle n_h \rangle^{1/3}$ roughly provide the limit of the reliability of estimating $P_i(k)$. The dark matter power spectrum $P(k)$ is estimated in two different methods. One is a direct estimate using the dark matter particles, $P^{\text{sim},r}(k)$. The other employs an analytical prescription by Peacock & Dodds (1996), $P^{\text{PD},r}(k)$. Upper-left panel of figure 5 shows these results. Symbols and curves represent the results using $P^{\text{PD},r}(k)$ and $P^{\text{sim},r}(k)$. Their agreement ensures the validity of the Peacock-Dodds prescription.

The wavenumber dependence of $1/b_1$ is weak for $k < 0.2h\text{Mpc}^{-1}$. The increase of $1/b_1$ for $k > 0.2h\text{Mpc}^{-1}$ is consistent with that expected from the halo finite volume exclusion effect (e.g., Taruya et al. 2001). When the wavenumber becomes comparable or larger than the mean separation of halos ($\sim 0.5h\text{Mpc}^{-1}$; c.f. Table 2), $P_i(k)$ does not represent the intrinsic clustering signal properly. Therefore the increase of $1/b_1$ against k may not be real for $k > 0.5h\text{Mpc}^{-1}$. In this paper we are interested in linear regimes where the k dependence of b_1 is negligible. Thus we do not consider the region $k > 0.2h\text{Mpc}^{-1}$, where the scale independent expansion like equation (4) breaks down.

In redshift space (s-cube in Table 2), we compute $P_i(k)$ using the center-of-mass peculiar velocity of each halo adopting the distant observer approximation. The dark matter power spectrum in *redshift space* is computed with two different methods. One is a direct estimate using the dark matter particles, $P^{\text{sim},s}(k)$. The other, $P^{\text{PD},s}(k)$, is an analytical prediction combining $P^{\text{PD},r}(k)$ and redshift distortion effects empirically. For the latter we consider the Kaiser effect (Kaiser 1987) and the finger-of-God effect assuming exponential peculiar velocity distribution (Cole et al. 1994; Cole et al. 1995; Kang et al. 2002). In this case the redshift space power spectrum is given as

$$P^{\text{PD},s}(k) = \left[A(\kappa_m) + \frac{2}{3}\beta_m B(\kappa_m) + \frac{1}{5}\beta_m^2 C(\kappa_m) \right] P^{\text{PD},r}(k), \quad (29)$$

$$A(\kappa_m) = \frac{1}{\kappa_m} \arctan(\kappa_m), \quad (30)$$

$$B(\kappa_m) = \frac{3}{\kappa_m^2} \left(1 - A(\kappa_m) \right), \quad (31)$$

$$C(\kappa_m) = \frac{5}{3\kappa_m^2} \left(1 - B(\kappa_m) \right), \quad (32)$$

where β_m denotes the value of equation (27) for dark matter particles, $\kappa_m = k\sigma_p/(\sqrt{2}H_0)$, and the rms pairwise velocity dispersion of dark matter particles, σ_p ($=\sqrt{2}\sigma_v \approx 520\text{km/s}$, σ_v is the one-dimensional velocity dispersion), is computed directly from N-body simulations. Upper-right panel in figure 5 displays the results for s-cube. Again b_1 is fairly scale independent in redshift space. Although the finger-of-God effect partially compensates the wavenumber dependence in r-cube for $k > 0.2h\text{Mpc}^{-1}$, $b_1(k)$ there is not reliable. The results of r-cube and s-cube imply that $b_1(k)$ is not sensitive to the redshift distortion, i.e., $b_1^s \approx b_1^r$ for $k < 0.2h\text{Mpc}^{-1}$. In fact, the agreement between $P^{\text{sim}}(k)$ and $P^{\text{PD}}(k)$ suggests that the above feature can be explained using equation (29):

$$\frac{b_{1,i}^s}{b_{1,i}^r} = \sqrt{\frac{A(\kappa_i) + \frac{2}{3}\beta_i B(\kappa_i) + \frac{1}{5}\beta_i^2 C(\kappa_i)}{A(\kappa_m) + \frac{2}{3}\beta_m B(\kappa_m) + \frac{1}{5}\beta_m^2 C(\kappa_m)}}, \quad (33)$$

where subscripts i and m refer to different subsamples and dark matter particles, respectively, and β_i indicates the value of equation (27) for each subsample, and $\kappa_i = k\sigma_{p,i}/(\sqrt{2}H_0)$. The rms pairwise velocity dispersion of halos, $\sigma_{p,i}$, is calculated from the simulated halo subsamples through $\sigma_p = \sqrt{2}\sigma_v$; 412 km/s for S and 397 km/s for L. Equation (33) yields 1.04 (0.97) at $k = 0.05h\text{Mpc}^{-1}$ and 1.08 (1.01) at $k = 0.2h\text{Mpc}^{-1}$ for the S (L) subsample. These values explain the behavior in figure 5 and suggest that b_1^s and b_1^r in linear regime agree within 10% level.

For wedge subsamples, we determine the positions of halos in redshift space properly using the line-of-sight velocity component unlike s-cube where we employ the distant observer approximation. In estimating $P_i(k)$, we follow Feldman, Kaiser & Peacock (1994), Matarrese et al. (1997) and Verde et al. (2002), and define the field:

$$F_i(\mathbf{r}) \equiv \lambda w(\mathbf{r})[n_i(\mathbf{r}) - \alpha n_r(\mathbf{r})], \quad (34)$$

where $w(\mathbf{r})$ is the weight, λ is a constant to be determined, $n_r(\mathbf{r})$ is the number density of random particles, $n_i(\mathbf{r})$ is the number density of each subsamples, and α is the ratio of particle numbers of actual and random catalogs. In this paper, $w(\mathbf{r})$ is unity inside the survey volume, and zero otherwise. If we set $\lambda = I_{22}^{-1/2}$, where

$$I_{jk} = \int d^3r w^j(\mathbf{r}) \bar{n}_i^k(\mathbf{r}) \quad (35)$$

with the mean number density \bar{n}_i for each subsample (Matarrese et al. 1997), then the power spectrum is

$$\langle |F_i(\mathbf{k})|^2 \rangle = P_i(k) + \frac{I_{21}}{I_{22}}(1 + \alpha) \quad (36)$$

(Verde et al. 2002). The dark matter power spectrum for the wedge subsamples is calculated by the two methods again: the first is an analytical calculation using equation (29) and the second is a direct estimation based on equation (36). The results are plotted in the lower-left panel of figure 5. Symbols correspond to the estimate using equation (28) with $P(k)$ evaluated from the Peacock-Dodds prescription. Solid and dashed lines use the direct estimate for $P(k)$, instead. They start to deviate at scales larger than the survey volume size itself. For $k > 0.1h\text{Mpc}^{-1}$ the estimate of b_1 in wedge configuration well reproduces that in s-cube, upper-right panel of figure 5.

Finally $b_1(k)$ for SDSS galaxies is computed similarly as wedge subsamples. In this case, however, we use the Peacock-Dodds prescription alone for simplicity. The lower-right panel of figure 5 is the result. The red (blue) sample is almost the same as L (S) in the lower-left panel. Lower-left panel of figure 5 is indeed in good agreement with the upper panels for $k < 0.2h\text{Mpc}^{-1}$, which we may interpret as an indication that the SDSS results in redshift space are directly related to their real-space property.

3.3. Bispectrum and Q

Finally we are in a position to consider the three-point statistics. We calculate the bispectra $B_i(k_1, k_2, k_3)$ using the same methods as $P_i(k)$ for r-cube and s-cube. For wedge and SDSS subsamples we use the formula

$$\langle F_i(\mathbf{k}_1) F_i(\mathbf{k}_2) F_i(\mathbf{k}_3) \rangle = \frac{I_{33}}{I_{22}^{3/2}} \left\{ B_i(\mathbf{k}_1, \mathbf{k}_2, \mathbf{k}_3) + \frac{I_{32}}{I_{33}} [P_i(\mathbf{k}_1) + P_i(\mathbf{k}_2) + P_i(\mathbf{k}_3)] + (1 - \alpha^2) \frac{I_{31}}{I_{33}} \right\} \quad (37)$$

(Verde et al. 2002). Figure 6 plots $Q_i(k)$, the reduced amplitude of bispectrum for equilateral triangles

$$Q_i(k) \equiv \frac{B_i(k, k, k)}{3P_i^2(k)}, \quad (38)$$

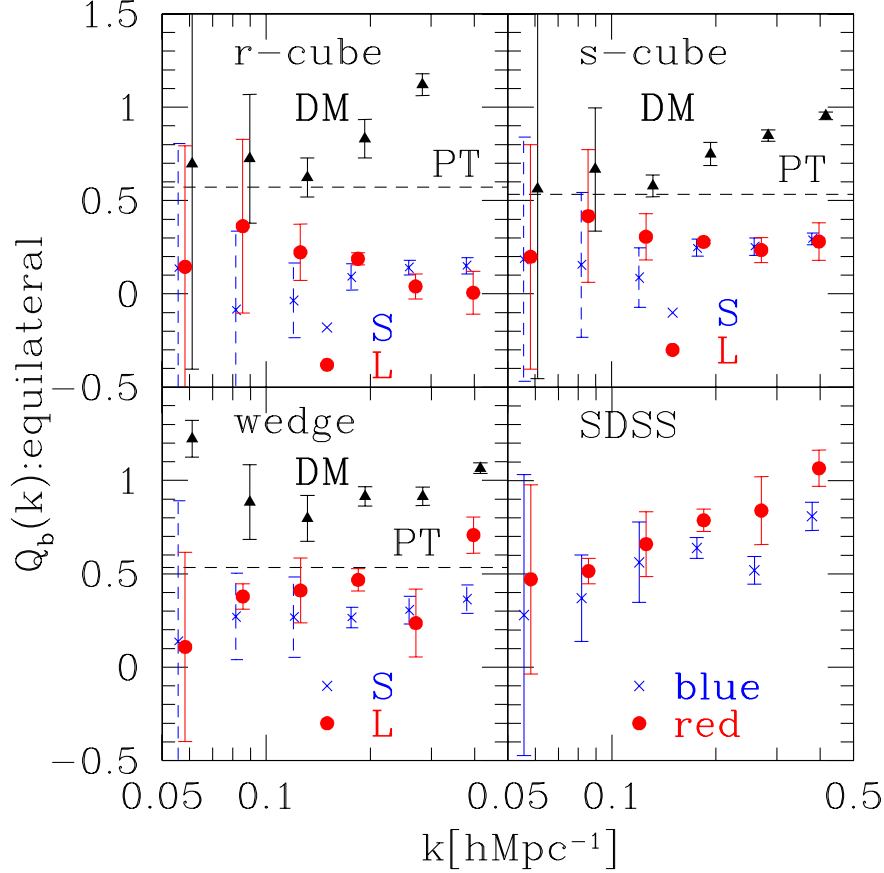


Fig. 6. Q_{halo} for simulated halos (Table 2) and Q_{galaxy} for SDSS galaxies (Table 1). Crosses and filled circles for simulated halos (SDSS galaxies) correspond to S and L samples (blue and red), respectively. For comparison, we also plot the value of Q_m calculated from N-body simulations (filled triangles) and from perturbation theory (PT, dashed lines) in r-cube, s-cube and wedge. The quoted error bars for simulated halos and dark matters are computed from three different realizations. We simply use the error bars for wedge subsamples just for reference in the case of SDSS galaxies.

which should be compared with figure 5. The difference of b_1 between the two different subsamples in each panel of figure 5 does not show up in figure 6. This is fully consistent with the finding of Kayo et al. (2004) for three-point correlation functions. Furthermore comparison among simulated halo subsamples indicates that this feature is not a simple outcome of the redshift distortion effect, but reflects the intrinsic correlation between b_1 and b_2/b_1 in real space as we discussed in section 2.

In order to proceed further, we attempt to estimate $b_2(k)/b_1(k)$ combining $Q_i(k)$ and $Q_m(k)$. We directly compute $Q_m(k)$ from simulation particles for r-cube, s-cube and wedge (filled triangles in fig.6). For comparison, tree-level perturbation theory predicts that

$$Q(k_1, k_2, k_3) = 2 \frac{F_2(\mathbf{k}_1, \mathbf{k}_2)P(k_1)P(k_2) + F_2(\mathbf{k}_2, \mathbf{k}_3)P(k_2)P(k_3) + F_2(\mathbf{k}_3, \mathbf{k}_1)P(k_3)P(k_1)}{P(k_1)P(k_2) + P(k_2)P(k_3) + P(k_3)P(k_1)}, \quad (39)$$

where we follow Jain & Bertschinger (1994) and define $F_2(\mathbf{k}_1, \mathbf{k}_2)$ as

$$F_2(\mathbf{k}_1, \mathbf{k}_2) = \frac{5}{7} + \frac{1}{2} \frac{\mathbf{k}_1 \cdot \mathbf{k}_2}{k_1 k_2} \left(\frac{k_1}{k_2} + \frac{k_2}{k_1} \right) + \frac{2}{7} \frac{(\mathbf{k}_1 \cdot \mathbf{k}_2)^2}{k_1^2 k_2^2}. \quad (40)$$

Strictly speaking, this expression of $F_2(\mathbf{k}_1, \mathbf{k}_2)$ is valid only for the Einstein-de Sitter universe, but its dependence on cosmology is proved to be very weak (Matsubara 1995; Scoccimarro et al. 1998). For equilateral triangles, equation (39) reduces to a constant value, $4/7$, which is plotted as a dashed line (PT) in the upper-left panel of figure 6 for real space. In redshift space, one obtains $Q = 0.533$ by setting $\gamma = 0$ and $\beta = \beta_m$ in the perturbation expression, equation (26), which is also plotted as a dashed line (PT) in the upper-right and lower-left panels. For $k < 0.2 h\text{Mpc}^{-1}$, the direct estimates (filled triangles; DM) agree with the perturbation values. In directly evaluating Q from N-body simulations, we use equation (8) for Q_m , and a similar expression for Q_i .

Figure 7 plots b_2/b_1 computed from

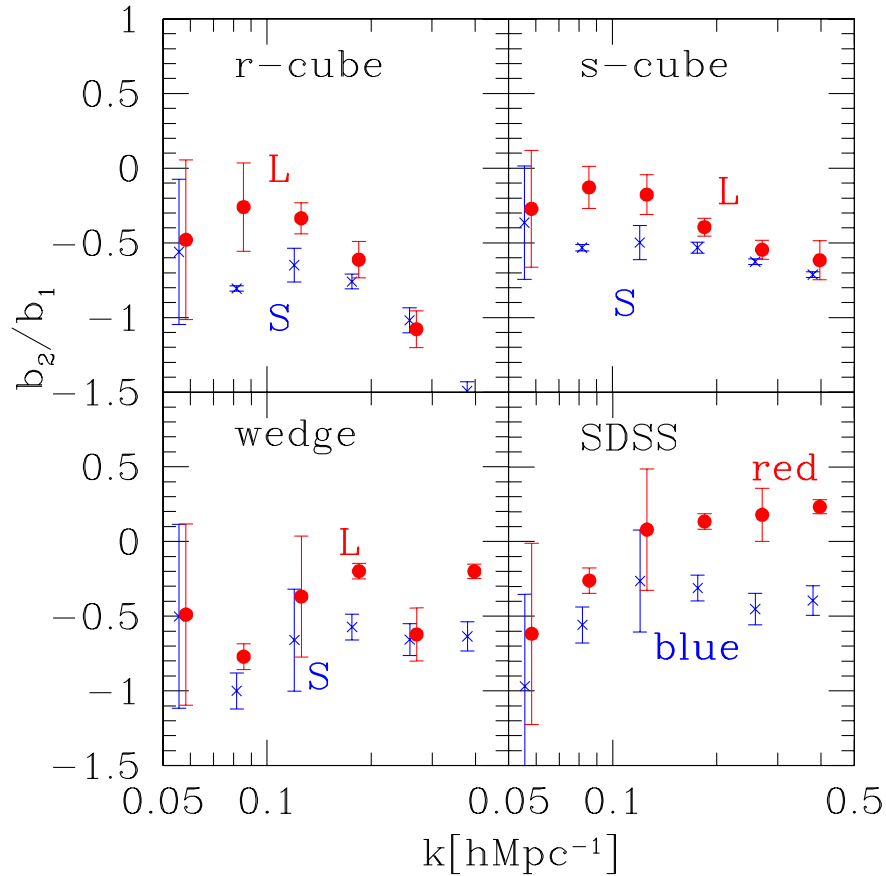


Fig. 7. b_2/b_1 for simulated halos (Table 2) and SDSS galaxies (Table 1). Crosses and filled circles for simulated halos (SDSS galaxies) correspond to S and L samples (blue and red), respectively. The quoted error bars for simulated halos are computed from three different realizations. We simply use the error bars for wedge subsamples just for reference in the case of SDSS galaxies.

$$(b_2/b_1)_i(k) \equiv b_{1,i}(k)Q_i(k) - Q_m(k). \quad (41)$$

For SDSS subsamples we use the value evaluated from wedge for $Q_m(k)$. Strictly speaking, equation (41) ignores redshift-space distortion effects. In reality, however, we made sure that almost the same values are derived even when we use equation (26) instead. Therefore we use equation (41) both in real- and redshift-space. Comparison between figure 5 and figure 7 indicates that subsamples with larger b_1 tend to have larger b_2/b_1 . This is consistent qualitatively with analytical results shown in figure 2.

To compare more quantitatively simulation results with analytic models, we average $b_{1,i}(k)$ and $(b_2/b_1)_i(k)$ over the range of $0.08h\text{Mpc}^{-1} < k < 0.2h\text{Mpc}^{-1}$. The results are plotted in the left panel of figure 8. The three curves show the analytic models plotted in figure 2 at $z = 0$, while squares correspond to the mass-averaged values for ellipsoidal halo model again in figure 2. Triangles, crosses, and circles, represent r-cube, s-cube, and wedge subsamples, respectively. If the analytic ellipsoidal halo model is exact, triangles and squares should agree within the error bars (we estimate from variance for three different realizations). The small differences between them may be ascribed to i) the inaccuracy of the higher order biasing coefficients in the halo model. The parameters (p and q) in equation (14) are empirically determined so as to reproduce the mass function but they do not guarantee the reliability for b_2 . ii) Weak scale dependence which is seen in figures 5 and 7. This is not expected in the analytic model, implying its practical limitation. iii) Inaccuracy of the estimators of b_1 and b_2/b_1 , and iv) stochasticity of biasing (DeKel & Lahav 1999; Taruya & Suto 2000; Taruya et al. 2001; Yoshikawa et al. 2001). The present halo model assumes deterministic biasing, which may affect the mean values of biasing coefficients, especially in the higher order. Given those realistic issues, we would interpret that triangles and squares are in reasonable agreement.

The right panel of figure 8 plots b_2/b_1 against b_1 for SDSS galaxy subsamples, which should be compared with the left panel for simulated halos. In addition to the color selected subsamples in Table 1, we construct nine luminosity threshold subsamples (Table 3) following Zehavi et al. (2005). We construct realistic galaxy mock samples in order to see if the observational data can be understood from simple theoretical modeling. We employ halo occupation distribution approach (HOD) which assigns galaxies within simulated halos. According to the simplest version of

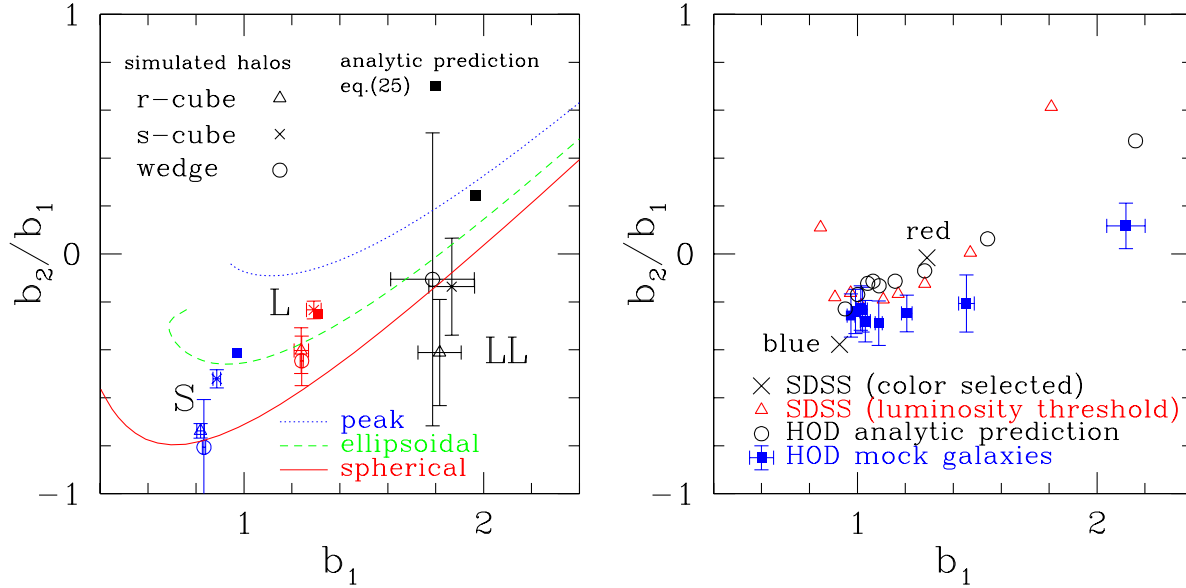


Fig. 8. Correlation between b_1 and b_2/b_1 . *left*: analytic models and simulated halos (Table 2). Lines are analytical predictions for spherical (solid), ellipsoidal (dashed) halo models, and peak model (dotted) as in figure 2 at $z = 0$. Squares are the mass averaged values corresponding to S and L subsamples for the ellipsoidal halo model. Other symbols are for halo subsamples. The quoted error bars are computed from three different realizations. *right*: SDSS color selected samples (Table 1; crosses), SDSS luminosity threshold samples (Table 3; triangles), HOD analytic prediction (circles), and HOD mock galaxies (Table 3; squares), and HOD analytic prediction (circles). Note that we do not distinguish b_n and B_n here.

Table 3. HOD parameters corresponding to the SDSS luminosity threshold galaxies

M_r^{\max}	z_{\min}	z_{\max}	$N_{\text{gal}}^{\text{SDSS}}$	$\log_{10} M_{\min}$	$\log_{10} M_1$	α	$\langle N_{\text{gal}}^{\text{mock}} \rangle$
-22.0	0.02	0.22	7704	13.91	14.92	1.43	1417
-21.5	0.02	0.19	24711	13.27	14.60	1.94	7235
-21.0	0.02	0.15	41969	12.72	14.09	1.39	28151
-20.5	0.02	0.13	69217	12.30	13.67	1.21	75292
-20.0	0.02	0.10	63770	12.01	13.42	1.16	141424
-19.5	0.02	0.08	56384	11.76	13.15	1.13	246421
-19.0	0.02	0.06	30532	11.59	12.94	1.08	365719
-18.5	0.02	0.05	24636	11.44	12.77	1.01	514269
-18.0	0.02	0.04	16123	11.27	12.57	0.92	745340

HOD, mean number of galaxies within halos of mass M is set as

$$\langle N(M) \rangle = \begin{cases} 1 + \left(\frac{M}{M_1} \right)^\alpha & M > M_{\min}, \\ 0 & \text{otherwise.} \end{cases} \quad (42)$$

In the above expression, the first term represents a central galaxy while the second corresponds to satellite galaxies. The three parameters, M_{\min} , M_1 , and α , are determined to reproduce the observed sample of galaxies. In practice, we adopt the values (Table 3) fitted by Zehavi et al. (2005) for the SDSS luminosity galaxies (see their Table 2). Their fit assumes the density profile proposed by Navarro, Frenk & White (1996) for galaxy distribution in each halo, and satellite galaxies within each halo are assigned following the Poisson distribution of the mean value of equation (42). We construct mock galaxy samples from our simulated halo catalogs using the routine of Skibba et al. (2006) which simultaneously takes care of the redshift-space distortion effect (see also Kang et al. 2005). In Table 3, $N_{\text{gal}}^{\text{SDSS}}$ and $\langle N_{\text{gal}}^{\text{mock}} \rangle$ denote the numbers of SDSS galaxy samples and the mean numbers of mock galaxy samples. Since the galaxy samples of Zehavi et al. (2005) are based on different galaxy catalog (SDSS DR2; Abazajian et al. 2004) from this work, the galaxy numbers of our luminosity threshold samples are about twice larger than theirs. We simply distribute mock galaxies in the simulation cubes and do not consider the survey boundary effect, so the numbers of mock galaxy samples do not correspond to those of SDSS galaxy samples.

According to the current HOD approach, we evaluate the biasing coefficients in two ways. One is an analytical estimate (HOD analytic prediction) which is based on equation (25):

$$B_n = \frac{\int_{M_{\min}}^{M_{\max}} dM n_{\text{halo}}(M, z=0) \langle N(M) \rangle b_n(M, z=0)}{\int_{M_{\min}}^{M_{\max}} dM n_{\text{halo}}(M, z=0) \langle N(M) \rangle}, \quad (n = 1, 2), \quad (43)$$

where we use the Sheth-Tormen mass function, equation (14), for $n_{\text{halo}}(M, z=0)$, and equation (20) for $b_n(M, z=0)$, and M_{\max} is set as the maximum mass of our simulated halos. The other is the direct evaluation of the biasing coefficients from the HOD mock galaxy samples using equations (28) and (41). The right panel of figure 8 plot these results for SDSS color selected samples (crosses), for SDSS luminosity threshold samples (triangles), for HOD analytic prediction (circles) and finally for HOD mock galaxies (squares with error bars). We note a few interesting features in the plot. i) The similarity between the color selected and luminosity threshold samples. While they are based on different selection criteria, the resulting $b_2/b_1 - b_1$ correlation seems to be roughly the same. ii) The HOD analytic prediction reproduces the values of b_2/b_1 and b_1 for each luminosity threshold galaxy samples. This is surprising since the fitting procedure is designed to reproduce their two-point correlation functions alone. iii) The discrepancy between the HOD mock and analytical results may come from the difference between Sheth-Tormen model and our halo samples in n_{halo} and/or b_2 . We made sure that n_{halo} of our halo samples is in good agreement with equation (14). On the other hand as the left panel of figure 8 indicates, b_2 for our simulated halos is systematically lower than the analytic prediction, equation (25). Thus the agreement between SDSS data and HOD models needs to be interpreted with caution. We also compute the values of b_2/b_1 and b_1 of HOD mock galaxy samples in real space. We, however, do not plot the results, since they are almost the same as those in redshift space.

Even with the above subtlety we find a fairly generic correlation between b_2/b_1 and b_1 , which is the most important result of the current study.

4. Summary and Discussion

We have found a fairly generic correlation between linear and quadratic biasing coefficients, b_1 and b_2/b_1 , using a variety of different methodologies; perturbative expansions of peak and halo biasing models, N-body simulations of halos, SDSS galaxy data analysis, and the corresponding halo occupation distribution predictions (analytic and mock). The presence of such correlations was suggested earlier by the previous finding that the normalized three-point correlation functions of SDSS galaxies in redshift space follow the hierarchical relation approximately, $Q = 0.5 \sim 1.0$, despite the robust morphological, color and luminosity dependences of the corresponding two-point correlation functions (Kayo et al. 2004). We have derived the $b_1 - b_2$ correlation explicitly and showed for the first time that it indeed explains the observed behavior of Q of SDSS galaxies in linear regimes.

The major findings of the present paper are summarized as follows.

- Even with the presence of redshift distortion and complicated survey shape effects, b_1 can be accurately estimated in $k < 0.2h\text{Mpc}^{-1}$. So b_1 estimated from SDSS galaxies is expected to reflect the true value in real space.
- The values of Q_b from simulated halos, mock galaxies based on HOD model, and SDSS galaxies do not show any clear dependence on b_1 . The independence on b_1 is not an artifact from the redshift-space distortion contamination, but is a consequence of the intrinsic correlation between b_2/b_1 and b_1 .
- The HOD model, equation (42), whose parameters are determined so as to reproduce the observed two-point statistics alone, seems to be also successful in predicting the value of b_2 .

There are a few remaining tasks which should be done following the present result. First, it is interesting to compare the current analysis in Fourier space with that in configuration space. As long as nonlinear effect is negligible, Q_m and Q_b in k-space are expected to be the same as those in configuration space. Nevertheless we would like to make sure of it, and to further explore the connection between bispectra and the three-point correlation functions of halos and galaxies. Second, the success of HOD to reproduce the correlation between b_2/b_1 and b_1 at the current level is very encouraging. Naturally it is important to further improve the HOD model. Third, the present paper considers only equilateral configuration of Fourier space triangles for Q . In reality, however, the different shape of triangles has a wealth of information. It is important to generalize the current analysis to an arbitrary shape of triangles in order to extract further information on the higher order biasing coefficients. The work along the line is now in progress.

We thank Akihito Shirata and Kohji Yoshikawa for useful discussions. The N-body simulations were performed at ADAC (Astronomical Data Analysis Center) of the National Astronomical Observatory, Japan. K. Y. and C. H. acknowledge the support from Grants-in-Aid for Japan Society for the Promotion of Science Fellows. This research

was partly supported by Grant-in-Aid for Scientific Research of Japan Society for Promotion of Science (No.16340053, 17740139).

Funding for the SDSS and SDSS-II has been provided by the Alfred P. Sloan Foundation, the Participating Institutions, the National Science Foundation, the U.S. Department of Energy, the National Aeronautics and Space Administration, the Japanese Monbukagakusho, the Max Planck Society, and the Higher Education Funding Council for England. The SDSS Web Site is <http://www.sdss.org/>.

The SDSS is managed by the Astrophysical Research Consortium for the Participating Institutions. The Participating Institutions are the American Museum of Natural History, Astrophysical Institute Potsdam, University of Basel, Cambridge University, Case Western Reserve University, University of Chicago, Drexel University, Fermilab, the Institute for Advanced Study, the Japan Participation Group, Johns Hopkins University, the Joint Institute for Nuclear Astrophysics, the Kavli Institute for Particle Astrophysics and Cosmology, the Korean Scientist Group, the Chinese Academy of Sciences (LAMOST), Los Alamos National Laboratory, the Max-Planck-Institute for Astronomy (MPIA), the Max-Planck-Institute for Astrophysics (MPA), New Mexico State University, Ohio State University, University of Pittsburgh, University of Portsmouth, Princeton University, the United States Naval Observatory, and the University of Washington.

References

- Abazajian, K., et al.2004, AJ, 128, 502 (Data Release Two)
- Adelman-McCarthy, J. K., et al.2006, ApJS, 162, 38 (Data Release Four)
- Bardeen, J. M., Bond, J. R., Kaiser, N., & Szalay, A. S. 1986, ApJ, 304, 15
- Bernardeau, F. 1994, A&A, 291, 697
- Blanton, M. R., Lin, H., Lupton, R. H., Maley, F. M., Young, N., Zehavi, I., & Loveday, J. 2003, AJ, 125, 2276
- Blanton, M. R., et al.2005, AJ, 129, 2562
- Bond, J. R., Cole, S., Efstathiou, G., & Kaiser, N. 1991, ApJ, 379, 440
- Bower, R. G. 1991, MNRAS, 248, 332
- Cole, S., Fisher, K. B., & Weinberg, D. H. 1994, MNRAS, 267, 785
- Cole, S., Fisher, K. B., & Weinberg, D. H. 1995 MNRAS, 275, 515
- Cooray, A., & Sheth, R. 2002, Phys. Rep., 372, 1
- Dekel, A. & Lahav, O. 1999, ApJ, 520, 24
- Eisenstein, D. J., et al.2001, AJ, 122, 2267
- Feldman, H. A., Kaiser, N., & Peacock, J. A. 1994., ApJ, 426, 23
- Fry, J. N., Gaztanaga, E. 1993, ApJ, 413, 447
- Fukugita, M., Ichikawa, T., Gunn, J. E., Doi, M., Shimasaku, K., & Schneider, D. P. 1996, AJ, 111, 1748
- Gunn, J. E., et al.1998, AJ, 116, 3040
- Gunn, J. E., et al.2006, AJ, 131, 2332
- Hamilton, A. J. S., & Tegmark, M. 2004, MNRAS, 349, 115
- Hikage, C., et al.2005, PASJ, 57, 709
- Hogg, D. W., Finkbeiner, D. P., Schlegel, D. J., & Gunn, J. E. 2001, AJ, 122, 2129
- Ivezić, Ž., et al.2004, Astron. Nachr., 325, 583
- Jing, Y. P., & Suto, Y. 1998, ApJ, 494, L5
- Jing, Y. P., & Suto, Y. 2002, ApJ, 574, 538
- Jain, B., & Bertschinger, E. 1994, ApJ, 431, 495
- Kaiser, N. 1987, MNRAS, 227, 1.
- Kang, X., Jing, Y. P., Mo, H. J., & Börner, G. 2002, MNRAS, 336, 892
- Kang, X., Jing, Y. P., Mo, H. J., & Börner, G. 2005, ApJ, 631, 21
- Kayo, I., et al.2004, PASJ, 56, 415
- Kitayama, T. & Suto, Y. 1996, ApJ, 469, 480
- Lupton, R., Gunn, J. E., Ivezić, Ž., Knapp, G. R., Kent, S., & Yasuda, N. 2001, in ASP Conf. Ser. 238, Astronomical Data Analysis Software and Systems X, ed. F. R. Harnden, Jr., F. A. Primini, and H. E. Payne (San Francisco: Astr. Soc. Pac.) 269
- Matarrese, S., Verde, L., Heavens, A. 1997, MNRAS, 290, 651
- Matsubara, T. 1995, Prog. Theor. Phys., 94, 1151
- Matsubara, T., & Suto, Y. 1994, ApJ, 420, 497
- Mo, H. J., Jing, Y. P., & White, S. D. M. 1997, MNRAS, 284, 189
- Mo, H. J., & White, S. D. M. 1996, MNRAS, 282, 347
- Navarro, J., Frenk, C., & White, S. D. M. 1996, ApJ, 462, 563
- Nichol, R. C., et al.2006, MNRAS, 368, 1507
- Peacock, J. A. & Dodds, S. J. 1996, MNRAS, 280, L19
- Pier, J., Munn, J. A., Hindsley, R. B., Hennessy, G. S., Kent, S. M., Lupton, R. H., Ivezić, Ž., for the SDSS collaboration, 2003, AJ, 125, 1559
- Press, W.H. & Schechter, P. 1974, ApJ, 187, 425
- Scoccimarro, R., Couchman, H., Frieman, J. A. 1999, ApJ, 517, 531
- Scoccimarro, R., Colombi, S., Fry, J. N., Frieman, J. A., Hivon, E., & Melott, A. 1998, ApJ, 496, 586
- Sheth, R. K., & Tormen, G. 1999 MNRAS, 308, 119
- Skibba, R., Sheth, R. K., Connolly, A. J., & Scranton, R. 2006, MNRAS, 369, 68
- Smith, J. A., et al.2002, AJ, 123, 2121
- Stoughton, C., et al.2002, AJ, 123, 485 (Early Data Release)
- Strauss, M. A., et al.2002, AJ, 124, 1810
- Suto, Y. 1993, Prog.Theor.Phys., 90, 1173
- Suto, Y., & Matsubara, T. 1994, ApJ, 420, 504
- Taruya, A., Magira, H., Jing, Y. P., & Suto, Y. 2001, PASJ, 53, 155
- Taruya, A. & Suto, Y. 2000, ApJ, 542, 559
- Tucker, D., et al.2006, AN, in Press
- Verde, L., et al.2002, MNRAS, 335, 432
- York, D. G., et al.2000, AJ, 120, 1579
- Yoshikawa, K., Taruya, A., Jing, Y. P., & Suto, Y. 2001, ApJ, 558, 520
- Zehavi, I., et al.2005, ApJ, 630, 1